Icarus 243 (2014) 91–103

Contents lists available at ScienceDirect

Icarus

journal homepage: www.elsevier.com/locate/icarus

Initial results from radio occultation measurements with the Mars Reconnaissance Orbiter: A nocturnal mixed layer in the tropics and comparisons with polar profiles from the Mars Climate Sounder

David P. Hinson [a,b,*], Sami W. Asmar [c], Daniel S. Kahan [c], Varoujan Akopian [c], Robert M. Haberle [d], Aymeric Spiga [e], John T. Schofield [c], Armin Kleinböhl [c], Wedad A. Abdou [c], Stephen R. Lewis [f], Meegyeong Paik [c], Sami G. Maalouf [c]

[a] Carl Sagan Center, SETI Institute, 189 Bernardo Ave., Mountain View, CA 94043, USA
[b] Department of Electrical Engineering, Stanford University, 350 Serra Mall, Stanford, CA 94305, USA
[c] Jet Propulsion Laboratory, California Institute of Technology, 4800 Oak Grove Drive, Pasadena, CA 91109, USA
[d] Space Science and Astrobiology Division, NASA Ames Research Center, Moffett Field, CA 94035, USA
[e] Laboratoire de Météorologie Dynamique, IPSL/UPMC/CNRS, 4 Place Jussieu, 75005 Paris, France
[f] Department of Physical Sciences, The Open University, Walton Hall, Milton Keynes MK7 6AA, UK

ARTICLE INFO

Article history:
Received 26 November 2013
Revised 20 August 2014
Accepted 11 September 2014
Available online 19 September 2014

Keywords:
Mars, atmosphere
Mars, climate
Atmospheres, dynamics
Meteorology

ABSTRACT

The Mars Reconnaissance Orbiter (MRO) performs radio occultation (RO) measurements on selected orbits, generally once per day. We have retrieved atmospheric profiles from two subsets of data, yielding a variety of new results that illustrate the scientific value of the observations. One set of measurements sounded the tropics in northern summer at a local time ~1 h before sunrise. Some of these profiles contain an unexpected layer of neutral stability with a depth of ~4 km and a pressure at its upper boundary of ~160 Pa. The mixed layer is bounded above by a temperature inversion and below by another strong inversion adjacent to the surface. This type of structure is observed near Gale Crater, in the Tharsis region, and at a few other locations, whereas profiles in Amazonis Planitia and Elysium Planitia show no sign of a detached mixed layer with an overlying inversion. We supplemented the measurements with numerical simulations by the NASA Ames Mars General Circulation Model, which demonstrate that water ice clouds can generate this distinctive type of temperature structure through their influence on radiative transfer at infrared wavelengths. In particular, the simulations predict the presence of a nocturnal cloud layer in the Tharsis region at a pressure of ~150 Pa (~10 km above the surface), and the nighttime radiative cooling at cloud level is sufficient to produce a temperature inversion above the cloud as well as convective instability below the cloud, consistent with the observations. The second set of measurements sounded mid-to-high northern latitudes in spring, when carefully coordinated observations by the MRO Mars Climate Sounder (MCS) are also available. The differences between the RO and MCS temperature profiles are generally consistent with the expected performance of the two instruments. Within this set of 21 comparisons the average temperature difference is less than 1 K where the aerosol opacities are smaller than 10^{-3} km^{-1}, at pressures of 10–50 Pa, whereas it increases to ~2 K where the aerosol opacities exceed this threshold, at pressures of 50–300 Pa. The standard deviation of the temperature difference is ~2 K, independent of pressure. The second set of RO measurements also provides unique information about the stability of the annual CO_2 cycle and the dynamics near the edge of the seasonal CO_2 ice cap.

1. Introduction

The Mars Reconnaissance Orbiter (MRO) has been performing radio occultation (RO) measurements since the primary science phase of the mission. We have begun to analyze these data, retrieving profiles of the neutral atmosphere and delivering them to the NASA Planetary Data System (PDS) for archiving and distribution. This paper describes the coverage of the measurements, the methodology, the characteristics of the retrieved profiles, and their scientific value. The atmospheric profiles derived from these data are comparable in quality to those obtained previously with Mars Global Surveyor (MGS) (Hinson et al., 1999, 2004) and concurrently

* Corresponding author at: Carl Sagan Center, SETI Institute, 189 Bernardo Ave., Mountain View, CA 94043, USA.
E-mail address: dhinson@seti.org (D.P. Hinson).

http://dx.doi.org/10.1016/j.icarus.2014.09.019
0019-1035/

with Mars Express (MEX) (Hinson et al., 2008a,b; Tellmann et al., 2013). Each spacecraft provides coverage at unique combinations of latitude, local time, and season, and the combined observations span ~8 martian years.

We report new results derived from two subsets of MRO RO observations, one from the tropics and the other from high northern latitudes. The former reveals the presence of an unexpected nocturnal mixed layer, while the latter yields a tight constraint on the stability of the annual CO_2 cycle. The discussion illustrates the value of sub-kilometer vertical resolution, precise determination of geopotential height, and other attributes of the RO retrievals. At the same time we validate the new observations by comparing them with previous RO measurements obtained with MGS under similar conditions.

We also compare the MRO RO measurements with profiles retrieved from carefully coordinated observations by the MRO Mars Climate Sounder (MCS) (McCleese et al., 2007; Kleinböhl et al., 2009). These two approaches to remote sensing rely on completely different physical principles, and the dissimilarity of the retrieval algorithms enhances the value of the comparisons. This is particularly true in the lower atmosphere, where aerosols can influence the MCS retrievals of temperature and pressure while the corresponding RO retrievals are insensitive to their effects. Our initial assessment is limited to a small set of observations obtained under conditions where both instruments are expected to yield reliable results. Overall we find a high degree of consistency between the MCS and RO temperature profiles, and we discuss the implications of the few outliers.

We follow established conventions for time keeping on Mars. The term 'sol' denotes the mean solar day of 88,775 s. Local time is expressed in true solar hours (24 per sol). The season is indicated by L_s, an angular measure of the position of Mars in its orbit, with $L_s \equiv 0^\circ$ at the vernal equinox of the northern hemisphere. In assigning numbers to years we adopt the convention that Mars year 1 (MY 1) began on 11 April 1955.

This paper is organized as follows. Section 2 describes the coverage of the MRO RO measurements and the manner in which they are implemented. Section 3 summarizes the quality of the data considered here, the method of analysis, and the characteristics of the retrieved profiles. In Section 4 we present the results derived from two subsets of RO data and explain their significance; three distinct topics are addressed. Section 4.1 discusses the nighttime temperature structure in the tropics and its response to radiative forcing by a water ice cloud layer. We rely on atmospheric models for guidance in interpreting these measurements; Sections 4.1.2 and 4.1.3 show selected results from a large-eddy simulation (LES) and a Mars General Circulation Model (MGCM), respectively. Section 4.2 describes measurements from northern spring at high northern latitudes, near the edge of the seasonal CO_2 ice cap. Section 4.3 reports detailed results derived from comparisons of MCS and RO temperature profiles. Section 5 updates the status of our ongoing analysis of the MRO RO measurements.

Color versions of Figs. 1, 4, 5, 7–9, 11, 12, 16, and 17 can be found in the web version of this article.

2. Observing plan

2.1. Coverage

MRO circles Mars in a low-altitude, Sun-synchronous, polar orbit, crossing the equator at local times of about 3 and 15 h (Zurek and Smrekar, 2007). Most orbits include geometric opportunities for radio occultation sounding of the martian atmosphere, and such observations have been performed routinely since early 2008. Fig. 1 shows their distribution in latitude, local time, and L_s, which complements and extends the RO coverage acquired by MGS (Hinson, 2006) and MEX (Tellmann et al., 2013).

The RO measurements are restricted to one orbit per day so as to minimize the impact on transmission of data collected by the primary scientific instruments onboard MRO. This sampling rate falls below the threshold of $\sim 6\ \mathrm{sol}^{-1}$ required for unambiguous identification of traveling waves on Mars (Banfield et al., 2004; Hinson et al., 2012). However, the number of orbits between successive observations is not uniform, which improves the spatial distribution of the measurements by dispersing their coverage in longitude.

Gaps of longer duration appear in Fig. 1 for several reasons. Occultations are absent when the orbital plane is nearly perpendicular to the Mars–Earth line, such as at $L_s = 29$–78° of MY 29 and $L_s = 63$–98° of MY 30. The observations are also curtailed by solar conjunction, near $L_s = 170^\circ$ of MY 29 and $L_s = 230^\circ$ of MY 30, when the data are corrupted by interference from plasma in the solar corona. Finally, anomalies disrupt spacecraft operations on some occasions, most notably from $L_s = 330^\circ$ of MY 29 to $L_s = 21^\circ$ of MY 30; this interruption began when the spacecraft entered safe mode in September 2009 and continued until normal operations had resumed in early December 2009.

2.2. Implementation

MRO is equipped with an ultra-stable oscillator (USO). Its performance is comparable to the ones carried by Voyagers 1 and 2 (Tyler, 1987) and the Galileo Orbiter (Howard et al., 1992), but it is less stable by a factor of ~10 than the one carried by MGS (Hinson et al., 1999; Tyler et al., 2001). Owing to the limited quality

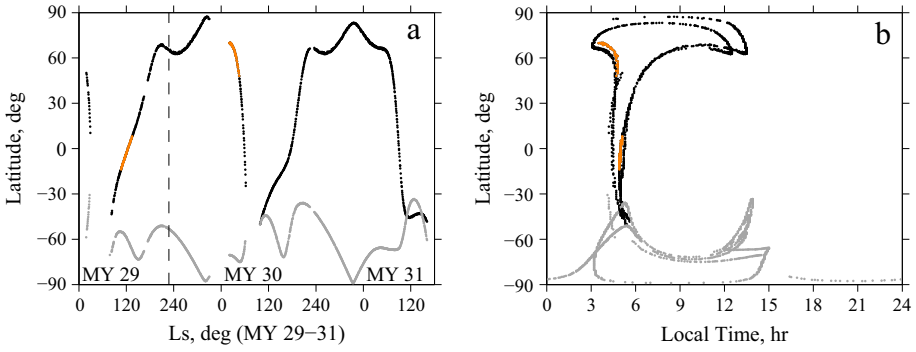

Fig. 1. Coverage of MRO RO observations from January 2008 ($L_s = 18^\circ$ of MY 29) through August 2012 ($L_s = 161^\circ$ of MY 31). Black and gray dots denote measurements at occultation entry and exit, respectively, whereas the two subsets of entry-side measurements discussed in this paper are shown in orange. The dashed vertical line denotes the start of coordinated observations by the MCS. (For interpretation of the references to color in this figure legend, the reader is referred to the web version of this article.)

of the MRO USO, the observations on the entry and exit sides of each occultation are implemented differently.

The entry-side RO measurements are conducted in a 'two-way' mode that avoids use of the USO. The spacecraft and ground equipment are configured as follows. A tracking antenna of the NASA Deep Space Network (DSN) transmits an unmodulated signal to MRO at a frequency of ~7.2 GHz (4.2 cm). Using the uplink signal as a frequency reference, MRO generates a downlink signal at a coherently-related frequency of ~8.4 GHz (3.6 cm) and relays it back to the tracking antenna on Earth, where the raw data are recorded. (The exact ratio of the two frequencies is 880/749.) A single hydrogen maser serves as the frequency reference for the signals transmitted and received by the DSN, enabling frequency measurements with the precision required for high-quality atmospheric sounding. This two-way mode has been employed successfully in previous entry-side RO observations with MEX (Hinson et al., 2008a,b; Tellmann et al., 2013).

The same approach is not suitable for measurements at occultation exit, where a coherent two-way link cannot be established quickly enough to prevent the loss of valuable observations of the lower neutral atmosphere. Instead, the exit-side measurements are conducted in a 'one-way' mode with the MRO USO serving as the frequency reference for the downlink signal. This strategy yields complete observations from the surface to the 'top' of the atmosphere, which come at the expense of a significant reduction in frequency stability.

The RO data are recorded by the DSN with operational guidance from the Radio Science Systems Group (http://radioscience.jpl.nasa.gov/) at the Jet Propulsion Laboratory. The RSSG gathers the raw data files from each observation and creates a set of archival data products, including Radio Science Receiver files (RSRs), Tracking and Navigation Files (TNFs), and Downlink Frequency Files (DLFs). Raw data from all the observations shown in Fig. 1 are currently available from the PDS Geosciences Node (ftp://pds-geosciences.wustl.edu/mro/mro-m-rss-1-magr-v1/mrors_0xxx/).

3. Data analysis

This paper reports results derived from two subsets of high-quality entry-side observations. One set of measurements sounded the tropics in summer of the northern hemisphere ($L_s \approx 120^\circ$ of MY 29) while the second set of measurements sounded high northern latitudes in spring ($L_s \approx 35^\circ$ of MY 30). We will designate these observations as groups A and B, respectively. We defer analysis of exit-side observations to a future publication.

3.1. Data quality

The quality of these RO measurements is not uniform. For the measurements in groups A and B, the difference arises from two sources.

The fundamental measurement is the change in signal frequency caused by the atmosphere of Mars. The magnitude of this change depends not only on the amount of refractive bending in the martian atmosphere but also on the orientation of the spacecraft velocity vector. For the orbit of MRO, the key geometric parameter is the angle between the spacecraft orbit plane and the direction to Earth, the so-called Earth out-of-plane angle (EOPA). The EOPA determines the size of the Doppler shift that results from a given amount of refractive bending, with a decrease in the EOPA producing an increase in the atmospheric Doppler shift and a commensurate improvement in the sensitivity of the measurements. For this reason the best observing geometry is a diametric occultation, where Earth is in the orbit plane and the EOPA is 0°, while a grazing geometry is less favorable.

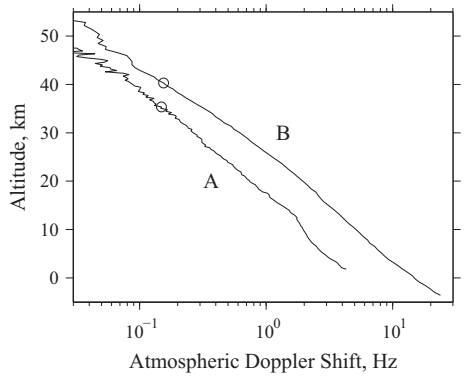

Fig. 2. Calibrated RO data from (A) 8 September 2008, when the EOPA was 57°, and (B) 27 December 2009, when the EOPA had decreased to 14°. The neutral atmosphere produces a Doppler shift that grows from roughly 40 mHz at 50 km altitude to roughly 10 Hz at the surface. Its magnitude at constant altitude is larger by a factor of 2–3 for the observation with the smaller EOPA. Altitude is measured from the reference areoid. Circles mark the top of the retrieved profiles of the neutral atmosphere.

This point is illustrated in Fig. 2, which compares the atmospheric Doppler shift associated with typical observations from groups A and B. The first case is a grazing equatorial occultation at $L_s = 124^\circ$ of MY 29 (group A), when the EOPA was 57°. In the second case, the occultation sounded high northern latitudes at $L_s = 29^\circ$ of MY 30 (group B), when the EOPA had decreased to 14° and the geometry was considerably closer to diametric. The atmospheric Doppler shift is larger by a factor of 2–3 for the observation with the smaller EOPA, and the measurements from group B are therefore less susceptible to errors arising from uncertainty in the reconstruction of the spacecraft trajectory and from unmodeled motion of the spacecraft high-gain antenna.

In addition to having a smaller value of the EOPA, the observations from group B have a second advantage over those from group A. The distance from MRO to Earth decreased from 2.4 au in early September 2008 (group A) to 0.8 au in late December 2009 (group B). The resulting increase in signal strength significantly reduced the effect of thermal noise on the profiles from group B.

For these two reasons, the uncertainties in pressure and temperature for the profiles from group A are generally about 50% larger than those from group B. The accuracy of the profiles is described in more detail in the next section.

3.2. Profile retrieval

Two-way measurements entail a more complicated observing geometry than one-way measurements. However, accurate profiles can be retrieved despite this increase in complexity (Jenkins et al., 1994), and the performance of the two-way retrieval algorithm has been validated with RO data from MEX (Hinson et al., 2008b, Fig. 1). Moreover, the geometry of the MRO observations is particularly favorable for two-way atmospheric sounding. Although the uplink and downlink signals follow different paths through the atmosphere of Mars, their separation is smaller than the characteristic Fresnel scale of diffraction effects, ~500 m in this case. The impact on the vertical resolution of the retrieved profiles is not significant.

The two-way retrieval algorithm is described by Hinson et al. (2008b). The initial steps of analysis make use of the Abel transform, which leads directly to a profile of refractive index versus planetocentric radius $\mu(r)$. The mixing ratios and refractive properties of the primary constituents of the lower atmosphere have been

measured independently, as summarized by Hinson et al. (1999), and we used that information to convert $\mu(r)$ to a profile of neutral number density $n(r)$. (For this mixture of gases the average refractive volume is 1.804×10^{-29} m^3.) The profile extends over the radial range $r_a < r < r_b$, where r_a is typically ~500 m above the surface and r_b is determined by data quality (see Fig. 2).

Profiles of pressure $p(r)$ and temperature $T(r)$ are derived from $n(r)$ by assuming hydrostatic balance, integrating vertically, and applying the ideal gas law. In a well-mixed atmosphere

$$T(r) = \frac{n_b T_b}{n(r)} + \frac{\bar{m}}{n(r)\,k} \int_r^{r_b} n(r')\,g(r')\,dr', \quad (1)$$

where $\bar{m}$ is the average molecular mass (7.221×10^{-26} kg), k is the Boltzmann constant, and g is the acceleration of gravity. Integration extends to radius r_b where the density n_b is known but the temperature T_b must be provided as a boundary condition. Note that the term involving T_b is inversely proportional to $n(r)$, so that its magnitude decays exponentially with increasing distance from the upper boundary.

The RO retrieval algorithm calculates the planetocentric radius r, east longitude λ, and latitude ϕ associated with each discrete sample of T and p. The uncertainty in position is generally less than ~10 m, commensurate with the accuracy of the MRO orbit reconstructions (P.R. Menon, personal communication, 2013). As the gravity field of Mars is well known (Konopliv et al., 2006), we can then compute the geopotential height Z at the location of each sample in the retrieved profile. This step also yields a convenient vertical coordinate, in which the geometric altitude z is measured relative to the equipotential surface that serves as the reference for martian topography (Smith et al., 2001). The pressure at $z = 0$ is typically about 500 Pa.

This method of analysis relies on standard formulas of geometrical optics (Fjeldbo et al., 1971), yielding profiles with a diffraction-limited vertical resolution of ~500 m for RO measurements with MRO. The horizontal resolution is constrained by the limb-sounding geometry. For the observations considered here, the downlink radio signal was traveling from southwest toward northeast as it passed near the surface of Mars. The horizontal resolution in this direction can be estimated as follows. The ray path traverses an atmospheric layer of depth d in a distance $L \approx 2\sqrt{2\,r_o\,d}$, where r_o is the radius at the base of the layer. When d is 3 km, the horizontal resolution L is ~300 km. (For comparison, 1° of latitude is 59 km.) The horizontal resolution in the direction perpendicular to the line of sight is comparable to the vertical resolution.

Each observation requires a baseline at altitudes where the effects of the neutral atmosphere and ionosphere are negligible. This baseline provides a reference for measuring the changes in signal frequency caused by the atmosphere of Mars, enabling accurate absolute calibration of the retrieved profile. In addition, information extracted from the baseline is needed for error analysis.

We now turn our attention to the accuracy of the RO measurements. Fig. 3 shows the errors associated with a typical profile from group B. The uncertainty in number density σ_n is a consequence of the noise inherent in the frequency measurements. This includes not only impulsive fluctuations, which arise from thermal noise, but also gradual variations, such as those caused by irregularities in the terrestrial ionosphere or by instability of the spacecraft attitude. We quantified their effects as follows. First, we characterized the properties of the noise through statistical analysis of data from the baseline interval. We then propagated the results through the RO retrieval algorithm, yielding the profile of σ_n that appears in Fig. 3a. In the example considered here, the standard deviation of the frequency fluctuations in the baseline is ~4 mHz, and the value of σ_n decreases from ~3% at the top of the profile, where p is 5 Pa, to ~0.02% at the base of the profile, where p is 840 Pa.

The retrievals of T and p are affected not only by the noise in the frequency measurements but also by the uncertainty in T_b, which is the predominant error source at pressures smaller than ~30 Pa. Fig. 3 characterizes the contributions from both sources when the 1-sigma uncertainty in T_b is set to 10 K. For the case considered here the total uncertainty in temperature σ_T decreases from 10 K (7%) at the top of the profile to 0.2 K (0.1%) near the surface.

4. Results and discussion

As of November 2013 we had delivered 103 atmospheric profiles to the PDS Atmospheres Node (http://atmos.nmsu.edu/MRO/mro.html), as summarized in Table 1. Fig. 1 shows their coverage

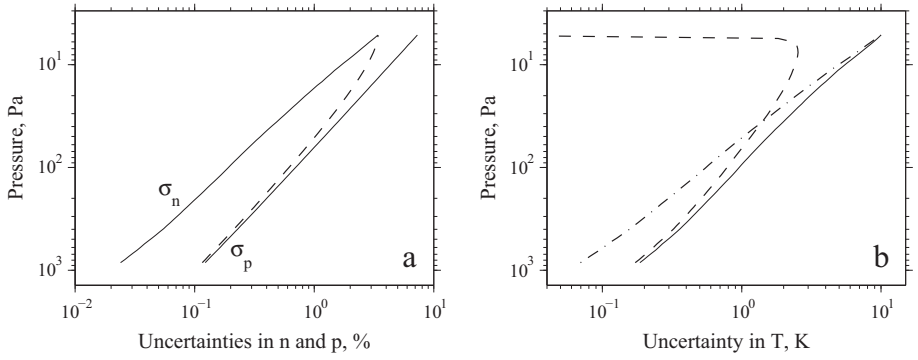

Fig. 3. The 1-sigma uncertainties for a typical profile from group B. The data were recorded on 27 December 2009; the same observation appears in Fig. 2. (a) The solid lines show the net uncertainties in number density (σ_n) and pressure (σ_p), while the dashed line shows the contribution to σ_p from the noise in the frequency measurements. The contribution to σ_p from the uncertainty in T_b is ~0.3 Pa, independent of pressure. (b) The solid line shows the net uncertainty in temperature, which comprises contributions from (dashed line) the noise in the frequency measurements and (dash-dotted line) the uncertainty in T_b.

Table 1
Coverage and other characteristics of MRO RO profiles delivered to the NASA PDS.

Group	Number of profiles	L_s/MY	Latitude	Local time	EOPA	Earth–Mars range
A	56	107–135°/29	14°S–8°N	4.8–5.0 h	59–57°	2.3–2.5 au
B	47	21–46°/30	69°N–48°N	3.6–4.8 h	6–42°	0.9–0.7 au

in latitude, local time, and L_s. Section 4.1 discusses observations of the tropics in summer of the northern hemisphere (group A), while Section 4.2 discusses observations at mid-to-high northern latitudes during spring (group B). In Section 4.3 we compare our results with profiles retrieved from coordinated observations by the MCS.

4.1. Tropical latitudes

Our initial results include 56 profiles from August–September 2008 (group A). These measurements sounded the atmosphere near the equator (14°S–8°N) during northern summer (L_s = 107–135° of MY 29) at a local time of ~5 h. The sampling in longitude is broad but not uniform, with a total of 22 profiles at longitudes of 90–180°E as compared with 8–16 profiles in the other quadrants. Within this set of observations, the uncertainty in T is typically ~1 K at the 400-Pa pressure level, near the surface, increasing to ~3 K at 50 Pa, where the altitude above the reference areoid is ~22 km.

This set of profiles was used previously to validate predictions of surface pressure at the landing site of the Mars Science Laboratory (MSL) in Gale Crater (Vasavada et al., 2012). Here we consider a different aspect of the results – a layer of neutral static stability that appears in some profiles within the lowest scale height above the surface. This section describes the characteristics of this distinctive feature and discusses a physical process that can produce a detached mixed layer at a local time ~1 h before sunrise. We rely on numerical simulations for guidance in interpreting the results.

4.1.1. Observations

In this discussion it is convenient to consider both the temperature T and the potential temperature θ, where

$$\theta \equiv T(p_o/p)^{R/c_p}. \quad (2)$$

The reference pressure p_o is set to 610 Pa. The exponent is the ratio of the gas constant R to the specific heat at constant pressure c_p; its value is ~0.25 for the conditions considered here. Profiles of θ give a clear indication of the static stability; the stratification is stable when $d\theta/dz > 0$ and unstable when $d\theta/dz < 0$.

Fig. 4 compares predawn profiles of θ from four widely separated locations in the tropics. Fig. 5 shows the same set of measurements as profiles of T, which emphasize other aspects of the vertical structure. Each profile contains a layer of neutral stability, with a depth of ~4 km, where θ is constant and the temperature

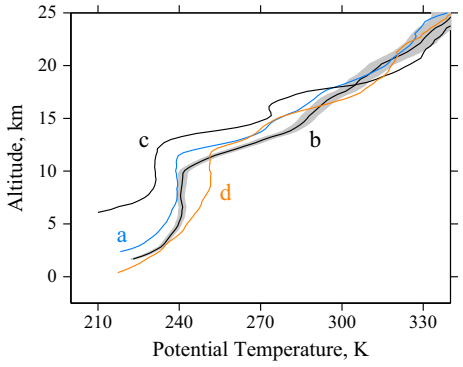

Fig. 4. MRO RO profiles of θ from four widely separated locations in the tropics: (a) 35°E, 4.7°S, (b) 125°E, 2.3°S, (c) 257°E, 2.2°S, and (d) 310°E, 4.9°N. The season is summer (L_s = 118–131°) and the local time is ~5 h. Each profile contains a detached mixed layer where θ is constant. The bottom of each profile is ~500 m above the surface. Altitude is measured from the reference areoid. The shaded region surrounding profile 'b' shows the typical 1-sigma uncertainty in θ for this set of observations.

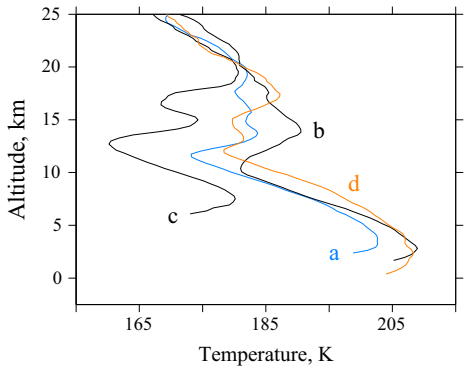

Fig. 5. Profiles of T for the same set of measurements as Fig. 4. The mixed layer in each profile resides between the mid-level and near-surface temperature inversions. The pressure at the top of the mixed layer is roughly 160 Pa.

lapse rate is adiabatic. The top of the mixed layer is marked by a distinct temperature minimum at an altitude of ~12 km, with an inversion of ~10 K at higher altitudes, as shown in Fig. 5. The bottom of the mixed layer is decoupled from the surface by a strong temperature inversion in the lowest few kilometers above the ground. The potential temperature in the mixed layer, the altitude of its lower and upper boundaries, and the detailed structure of the overlying inversion vary noticeably among these four profiles. The variability is largest at altitudes below 20 km, where the measurements are most reliable, whereas the four profiles converge at higher altitudes. Fig. 6 marks the locations of these four profiles, as well as the ones shown in Figs. 7–9, on a map of surface topography.

Condensation of water vapor releases latent heat, a process ignored by Eq. (2), and we now assess its impact on stability. (The reason for this digression will become clear in Section 4.1.3.) It is sufficient to consider the limiting case where the atmosphere is saturated with water vapor at all altitudes. Under these conditions the generalized form of Eq. (2) that accounts for latent heat is given by

$$\theta_e \approx \theta \exp[(L_v q_w)/(c_p T)], \quad (3)$$

where θ_e is the equivalent potential temperature, as discussed by Gill (1982), L_v is the latent heat of sublimation for water ice, and q_w is the mass mixing ratio of water vapor for a saturated atmosphere. For the observations in Fig. 4, the difference between θ_e and θ is typically ~0.3 K within the nocturnal mixed layer, where $d\theta_e/dz$ is smaller than $d\theta/dz$ by ~ 0.1K km^{-1}. At these temperatures the vapor pressure of water is too small for latent heat to have a significant effect on stability.

Within this set of measurements, there is a close resemblance among profiles retrieved from nearly the same location on different sols. For example, Fig. 7 examines the sol-to-sol variability at two locations, one centered at 131°E, 2.0°S in northern Terra Cimmeria, and another centered at 176°E, 0°N in southeastern Elysium Planitia. (The first location is a few hundred kilometers northwest of the MSL landing site in Gale Crater.) The vertical structure in both regions is highly repeatable from sol to sol.

Fig. 7 also shows that the mixed layer is a regular feature of the predawn vertical structure at some locations, such as near Gale Crater, while it is absent at others. The resulting zonal variations in θ, which reach ~15 K at 10 km altitude, are significantly larger than the sol-to-sol variability at either location. Within this subset of measurements, the surface elevation is higher by ~3 km where the mixed layer appears.

Motivated by these results, we searched for the same phenomenon in MGS RO profiles acquired under similar conditions in pre-

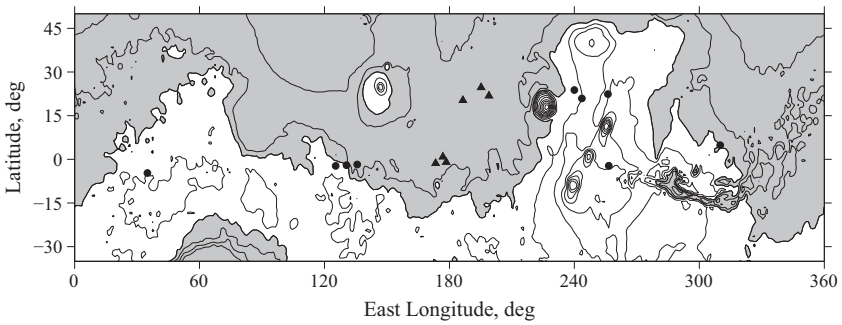

Fig. 6. Locations of the measurements shown in Figs. 4, 5, and 7–9, including subsets of observations by both MRO (5°S–5°N) and MGS (20–25°N). A detached nocturnal mixed layer is present at locations marked by circles, whereas the feature is absent at locations marked by triangles. Surface elevation is shown by contours, with a separation of 2 km at elevations below +10 km and 2.5 km at higher elevations. Shading denotes negative elevation.

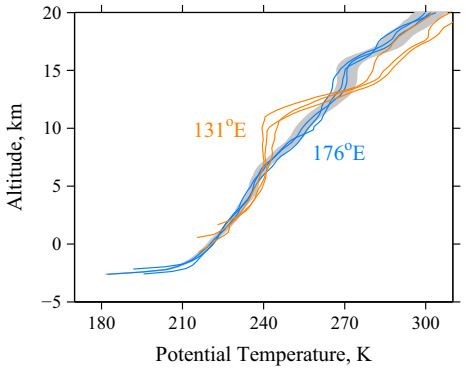

Fig. 7. MRO RO profiles from two regions in the tropics. The season is northern summer ($L_s = 121–126°$). The orange lines show profiles from observations on 3 consecutive sols in northern Terra Cimmeria (125°E, 2.3°S; 131°E, 2.0°S; 136°E, 1.7°S). The blue lines show 3 profiles from contemporaneous observations in southeastern Elysium Planitia (173°E, 1.3°S; 179°E, 0.9°S; 177°E, 0.9°N). The local time is ~5 h. The shaded region surrounding the profile at 173°E shows the typical 1-sigma uncertainty in θ for this set of observations. (For interpretation of the references to color in this figure legend, the reader is referred to the web version of this article.)

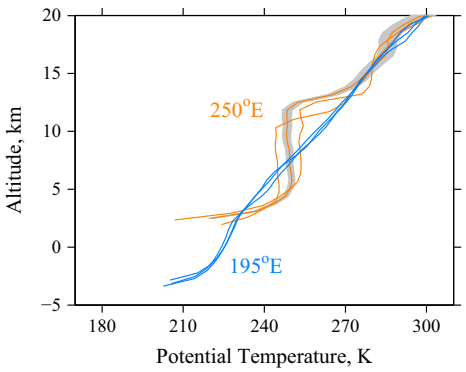

Fig. 8. MGS RO profiles from two regions in the tropics. The season is northern summer ($L_s = 139–140°$). The orange lines show profiles from observations on 3 consecutive sols in the northern Tharsis region (240–260°E, 20–25°N). The blue lines show 3 profiles from contemporaneous measurements in Amazonis Planitia (185–205°E, 20–25°N). The local time is 4.2 h. A detached mixed layer, where θ is constant, appears above Tharsis but not in Amazonis. The shaded region surrounding one of the Tharsis profiles shows the typical 1-sigma uncertainty in θ for this set of observations. (For interpretation of the references to color in this figure legend, the reader is referred to the web version of this article.)

vious years. A nocturnal mixed layer appears in some of the MGS profiles, though it had been largely overlooked until now. The initial results from MRO can be compared readily with MGS measurements from northern summer of MY 24, which sounded the

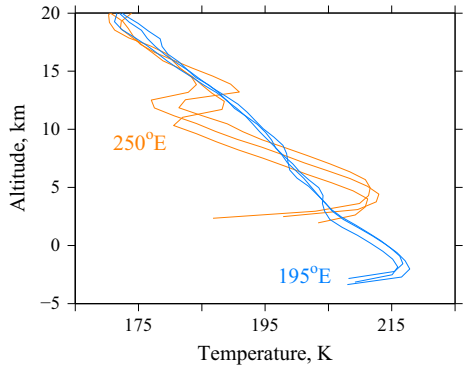

Fig. 9. Profiles of T for the same set of measurements as Fig. 8. The Tharsis profiles, shown in orange, contain a mixed layer capped by a temperature inversion. Both features are absent from the Amazonis profiles, shown in blue. The bottom of each profile is ~500 m above the surface. (For interpretation of the references to color in this figure legend, the reader is referred to the web version of this article.)

atmosphere at a similar combination of latitude, local time, and L_s. This is the best opportunity for cross calibration of RO observations in the tropics by the two spacecraft.

A broad examination of the MGS profiles is beyond the scope of this paper. Our immediate goals can be achieved by limiting the discussion to results from two regions, one in Amazonis (185–205°E, 20–25°N) and another between Tharsis Montes and Alba Patera (240–260°E, 20–25°N). MGS sounded each region three times during a 4-sol span of observations in northern summer ($L_s = 139–140°$ of MY 24). The results appear in Figs. 8 and 9. The local time for all six profiles is 4.2 h, nearly 1 h earlier than the MRO profiles in Figs. 4, 5, and 7.

The MGS profiles in Figs. 8 and 9 exhibit the same characteristic features as their counterparts from MRO. There is a strong resemblance among measurements on successive sols at nearly the same location. A detached mixed layer appears regularly at some locations, such as the Tharsis region, but not others, such as Amazonis. The mixed layer is capped by a temperature inversion of ~10 K in each of the Tharsis profiles. The absolute values of T and θ observed by the two spacecraft also appear to be mutually consistent, although a quantitative comparison is hindered by differences in the longitude, latitude, season, and local time of the measurements. These similarities strengthen our confidence in the accuracy of the MRO and MGS profiles, while demonstrating that the nocturnal mixed layer is not unique to MY 29.

4.1.2. Large-eddy simulations of the diurnal cycle

The structure and dynamics of the daytime convective boundary layer (CBL) have been investigated with high-resolution

numerical simulations (Michaels and Rafkin, 2004; Spiga et al., 2010). But the behavior at nighttime within this region of the atmosphere – the lowest scale height above the surface – has attracted less attention from atmospheric modelers. In this section we supplement the previous studies through use of large-eddy simulations (LES) of the full diurnal cycle, providing a context for interpreting nighttime observations at fixed local time.

We performed these simulations with the Martian Mesoscale–Microscale Model of the Laboratoire de Météorologie Dynamique (Spiga and Forget, 2009), which combines a fully compressible non-hydrostatic dynamical core with a 10-layer soil model for computing surface temperature and a detailed parameterization of radiative transfer by atmospheric dust and CO_2. In most respects the conditions considered here are the same as in a previous application of the LMD model by Spiga et al. (2010); only the duration and the season of the simulations have changed. We ran the model on a grid with 121 samples in the vertical direction and 201 samples in both horizontal directions, with an isotropic grid spacing of 100 m, so that the domain size is $12 \times 20 \times 20$ km. The dust loading is horizontally uniform with column opacity of 0.3, the atmosphere is dry and cloud free, and each simulation begins with an atmosphere at rest.

First we consider a location in Amazonis Planitia (205°E, 14°N) that was investigated previously by Spiga et al. (2010, case b of Table II). We adopt the same values for the surface properties as in the preceding study. Our simulation extends through a full diurnal cycle at $L_s = 140°$, the same season as the MGS profiles in Figs. 8 and 9.

Fig. 10 shows selected profiles of θ from the LES in Amazonis. The daytime profiles are statically unstable ($d\theta/dz < 0$) within a shallow layer adjacent to the surface, where the atmosphere is heated primarily by surface long-wave radiation (Michaels and Rafkin, 2004). The potential temperature within this shallow surface layer increases from ~195 K at 08 h to ~240 K at 15 h, creating positive buoyancy that drives convection at higher altitudes throughout the day. The resulting mixed layer, where θ is nearly constant, appears shortly after sunrise and its depth grows steadily from less than 1 km at 09 h to ~6 km at 15 h, as shown in Fig. 10a. The LES prediction for the depth of the mixed layer in late afternoon is confirmed by MEX RO measurements at this location (Hinson et al., 2008a; Spiga et al., 2010).

The daytime CBL achieves its maximum depth, ~6 km at this location and season, at a local time near 16 h. The subsequent rapid decrease in surface temperature, which continues throughout the night, removes the forcing for convective activity. In response to nighttime radiative cooling, the lower atmosphere returns to stable stratification, with the static stability $d\theta/dz$ increasing steadily until sunrise, as shown in Fig. 10b.

The nighttime profiles in Fig. 10b retain a change in slope at an altitude of 2–3 km, near the peak height of the daytime CBL. The three Amazonis profiles in Fig. 8 exhibit this feature – as noted previously by Fenton and Michaels (2011) – confirming this aspect of the simulation. Hence, we find that the results from the LES in Amazonis are consistent with both daytime measurements by MEX and nighttime measurements by MGS.

We performed an analogous numerical simulation in the Tharsis region (237°E, 12°N) at another of the locations investigated previously by Spiga et al. (2010, case c of Table II). The surface elevation is ~6 km higher than in Amazonis and the LES produces a deeper CBL, consistent with late afternoon measurements by MEX at this location (Hinson et al., 2008a; Spiga et al., 2010). In all other respects the diurnal cycle in the Tharsis simulation (not shown) closely resembles the one in Amazonis, with no sign in the nighttime profiles of either a detached layer of neutral stability or a mid-level temperature inversion.

In summary, the LES performs well in Amazonis but it cannot explain the peculiar nighttime structure observed in the Tharsis region. A key physical process is missing from the version of the LES used in these calculations. Possibilities include the radiative effects of water ice clouds and dynamical forcing associated with planetary-scale variations in topography. We now turn our attention to these topics.

4.1.3. MGCM simulations of the radiative effects of water ice clouds

In this section we discuss the impact of water ice clouds on the nighttime temperature structure in the tropics. We demonstrate that clouds can produce the features of interest – a mixed layer capped by a temperature inversion – through their influence on radiative transfer at infrared wavelengths.

We ascribe the overlying temperature inversion to nighttime radiative cooling by a water ice cloud layer. The cold trap at the base of the inversion is conducive to cloud formation, while thermal emission from the ice particles causes further cooling at cloud level, creating positive feedback. Numerical simulations have demonstrated the importance of this interaction to the formation of nighttime temperature inversions in the tropics (Haberle et al., 1999; Colaprete and Toon, 2000; Hinson and Wilson, 2004; Wilson and Guzewich, 2014).

Moreover, we find strong support for this interpretation in the latest results from the MRO MCS (Wilson and Guzewich, 2014). Through analysis of equatorial profiles of temperature and water ice opacity, Wilson and Guzewich have shown that the climate of Mars is characterized by the seasonal appearance in the Tharsis region of an elevated nocturnal cloud layer embedded within a deep temperature inversion. This distinctive type of nighttime structure recurs above Tharsis throughout the aphelion season

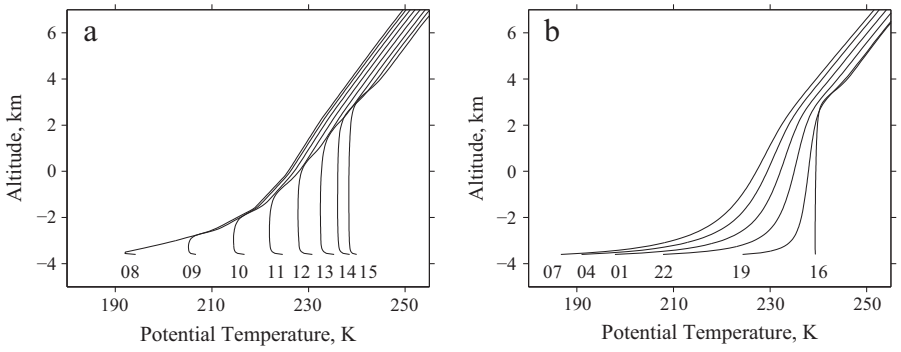

Fig. 10. Profiles of θ from the LES in Amazonis at 205°E, 14°N. The season is summer, $L_s = 140°$. These profiles have been averaged over the horizontal domain of the LES. (a) Daytime profiles at 1-h intervals of local time from 08 to 15 h. (b) Nighttime profiles at 3-h intervals from 16 to 07 h. We have omitted (a) 2 samples and (b) 4 samples from the bottom of each profile for clarity. The surface elevation at this location is −3.6 km.

($L_s \approx 0$–150°) in three successive years of MCS observations (MY 29–31). The same Tharsis inversion appears in concurrent RO measurements by MRO in MY 29, as shown in profile 'c' of Fig. 5, and the MCS observations confirm that a cloud layer resides within this equatorial inversion.

What's new about the observations in Section 4.1.1 is the further implication that radiative cooling at cloud level can induce convective instability below the cloud. In this scenario, the predawn mixed layer is driven from above by negative buoyancy, which arises from radiative cooling in an overlying water ice cloud.

We tested this hypothesis by performing numerical simulations with the NASA Ames Mars General Circulation Model (MGCM), using the configuration described by Haberle et al. (2011). This version of the model employs a terrain following sigma coordinate with 40 layers extending from the surface to an altitude of ~80 km. The horizontal resolution is 5° in latitude by 6° in longitude, comparable to the footprint of Olympus Mons and the horizontal resolution of the RO measurements. Key attributes of the model include a detailed representation of the water cycle; a microphysics module that tracks the nucleation, condensation, sublimation, and sedimentation of water ice aerosols; a Van Leer formulation of aerosol transport; a two-stream approximation for radiative transfer that accounts for both gases and aerosols; a level-2 Mellor–Yamada parameterization of turbulent mixing in the planetary boundary layer; and a subsurface module that incorporates heterogeneous soil properties. The model uses smoothed maps of surface properties – topography, thermal inertia, and albedo – derived from observations by MGS and the Viking Orbiters. In the simulations considered here the dust distribution is constrained to match the column opacity observed by the MGS Thermal Emission Spectrometer (TES) in MY 26–27.

We characterized the impact of water ice clouds on the temperature structure in the tropics by comparing the results from two MGCM simulations. In our baseline simulation the clouds are passive in the sense that their effect on radiative transfer is ignored. In the second simulation the clouds are radiatively active, with the model accounting for their interaction with radiation at both visible and infrared wavelengths. This approach has been used previously with the Ames MGCM to study the effects of radiative forcing by water ice clouds on key aspects of martian weather and climate, such as the water cycle (Haberle et al., 2011), the dust cycle (Kahre et al., 2011), and atmospheric dynamics at high latitudes (Hollingsworth et al., 2011).

Fig. 11 shows selected results from the two simulations. These profiles are from the Tharsis region at 234°E, 10°N – about midway between Olympus Mons and Pavonis Mons – at the same local time (4 h) and season ($L_s = 140^\circ$) as the observations in Figs. 8 and 9. The MGCM predicts the presence of a water ice cloud layer with a sharp lower boundary at an altitude of ~10 km, as shown in Fig. 11a. The cloud layer is largely nocturnal at this location, with a cloud mass that peaks near midnight and becomes negligible around midday (not shown). In the 'radiatively active' simulation, this nocturnal cloud layer emits more infrared radiation than it absorbs – a consequence of the deep nighttime reduction in thermal emission from the surface – thereby cooling the atmosphere at cloud level. The relatively low surface thermal inertia in the Tharsis region enhances this effect (Wilson and Guzewich, 2014).

The temperature structure changes significantly when the cloud is radiatively active, as shown in Fig. 11b. Nighttime radiative cooling at cloud level (11–16 km) reduces temperatures by ~5 K relative to the baseline simulation, producing a weak temperature inversion above the cloud layer and triggering convective instability below the cloud. The mixed layer is more easily identified in Fig. 12, which shows profiles of θ from the two simulations. Note that the cloud structure responds to the changes in the temperature profile, resulting in a cloud layer that tends to be more sharply peaked and narrowly confined when the cloud is radiatively active.

Both the nocturnal mixed layer and the overlying temperature inversion are absent from the simulation with passive clouds. Hence, both features originate primarily from cloud radiation. Dynamical forcing, which could arise for instance from shear instability in the nocturnal jet, does not appear to be important, at least at the location considered in Figs. 11 and 12. The latent heat released during cloud formation is likewise not significant; the

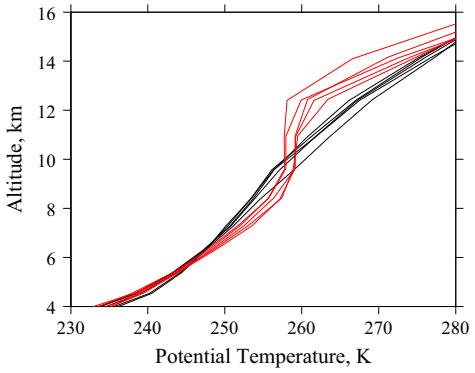

Fig. 12. Profiles of θ from MGCM simulations in the Tharsis region. The corresponding profiles of T appear in Fig. 11b. The red profiles are from a simulation with radiatively active water ice clouds, whereas the black profiles are from a baseline simulation with passive clouds. (For interpretation of the references to color in this figure legend, the reader is referred to the web version of this article.)

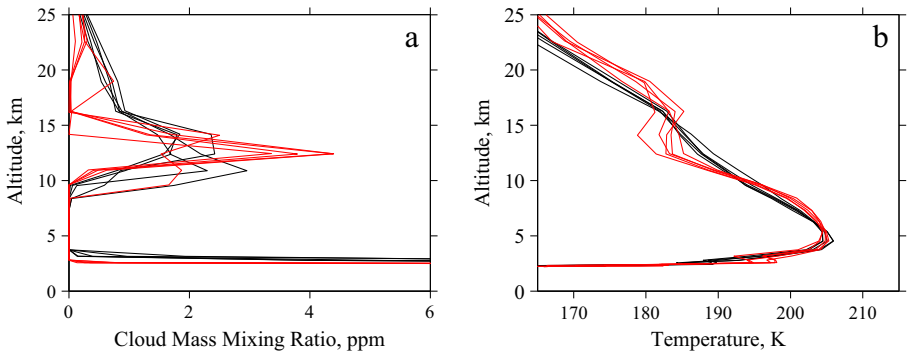

Fig. 11. Profiles of (a) cloud mass mixing ratio and (b) T from MGCM simulations in the Tharsis region at 234°E, 10°N. The season is northern summer, $L_s = 140^\circ$. The red profiles are from a simulation with radiatively active water ice clouds, whereas the black profiles are from a baseline simulation with passive clouds. Results are shown from five successive sols at a fixed local time of 4 h, when the surface temperature is approaching its diurnal minimum. The surface elevation at this location is +2.2 km. (For interpretation of the references to color in this figure legend, the reader is referred to the web version of this article.)

resulting change in temperature is smaller than 0.1 K for the clouds shown in Fig. 11a, as estimated from Eq. (26) of Zurek et al. (1992).

The simulation with radiatively active water ice clouds is able to account for key features of the MGS observations in the Tharsis region, but there are some notable differences as well. The simulated inversion is less pronounced than the one in the observations. In addition, the mixed layer has a depth of 1–2 km in the simulation as compared with 5–6 km in the observations. These discrepancies suggest that the MGCM may be underestimating the opacity of the cloud layer.

Nonetheless, the simulations confirm our basic hypothesis – radiatively active water ice clouds can produce a nighttime mixed layer capped by a temperature inversion. While the fundamental radiative forcing for this process is well understood from previous numerical simulations (Madeleine et al., 2012; Wilson et al., 2014; Wilson and Guzewich, 2014), our results provide a more complete description of its impact on the nighttime temperature structure.

4.1.4. Regional variations in atmospheric structure

Previous MGCM simulations have shown that thermal tides shape the spatial distribution and diurnal evolution of water ice clouds, while cloud radiation can intensify the tides (Hinson and Wilson, 2004; Madeleine et al., 2012). Observations by the MCS support these conclusions (Lee et al., 2009; Heavens et al., 2010). This tide-cloud coupling contributes to the formation of nighttime temperature inversions in the tropics during the aphelion season, which are a conspicuous feature of MGS RO measurements (Hinson and Wilson, 2004) and more comprehensive measurements by the MCS (Wilson and Guzewich, 2014). In both sets of observations, the strongest inversions appear near the equator in the Tharsis region, where planetary-scale topographic forcing produces a local enhancement in the amplitude of the diurnal tide (Hinson and Wilson, 2004).

As noted in Section 4.1.1, there is a close resemblance among profiles from different sols at essentially the same location, but the vertical structure varies considerably from one region to another (see Figs. 7–9). Planetary-scale variations in topography contribute to this pattern of behavior through their impact on the thermal tides (Hinson and Wilson, 2004), as discussed in the preceding paragraph. However, the vertical wavelength of the Sun-synchronous diurnal tide, ~35 km, far exceeds the vertical scale of the Tharsis inversions in Fig. 9. This suggests that another atmospheric process plays a significant role in determining the regional distribution and vertical structure of nighttime water ice clouds along with the characteristics of the temperature inversions and mixed layers.

In this regard the influence of the convective boundary layer should not be overlooked. Planetary-scale variations in topography modify the dynamics in the lowest scale height above the surface in several important ways. First, MEX RO measurements in late afternoon have shown that the CBL is deep (8–10 km) where the surface elevation is high, as in the Tharsis region, and shallow (4–6 km) where the surface elevation is low, as in Amazonis (Hinson et al., 2008a; Tellmann et al., 2013). The resulting difference in the altitude at the top of the daytime CBL is more than 8 km. Second, large-eddy simulations have shown that daytime convection is not only deeper above Tharsis but also considerably more intense than it is in Amazonis (Spiga et al., 2010). Finally, the surface elevation in the Tharsis region is ~6 km higher than in Amazonis, whereas the daytime surface temperatures are comparable in the two regions, so that the Tharsis region acts as an elevated heat source.

These topographic effects are expected to enhance the vertical mixing of water vapor above elevated terrain, which may be conducive to nighttime cloud formation within these regions. This could help account for the distinctive regional variations in atmospheric structure (Figs. 7–9). We note that substantial nighttime water ice clouds appear in the aphelion season, as revealed by other MGS observations, and that the nighttime cloud opacity is largest where the surface elevation is high, in the Tharsis region and Syrtis Major (Wilson et al., 2007; Pankine et al., 2013).

We plan to explore these phenomena in greater detail through further analysis of high-resolution RO temperature profiles and MCS profiles of water ice opacity. The cumulative RO coverage by MGS, MEX, and MRO already includes both daytime and nighttime observations in the tropics at a range of seasons, while MCS profiles of water ice opacity are available at local times of 3 and 15 h with systematic coverage in latitude, longitude, and L_s. The immediate goal is to derive a more complete characterization of the lowest scale height of the tropical atmosphere – its spatial structure, diurnal variations, and seasonal evolution. The results will also provide new constraints for large-eddy simulations, mesoscale models, and MGCMs.

4.2. High northern latitudes

We have retrieved 47 atmospheric profiles from RO measurements acquired during December 2009 and January 2010 (group B). These measurements sounded the atmosphere in spring, $L_s = 21–46^\circ$ of MY 30, drifting in latitude from 69°N at the start of the interval to 48°N at the end, as shown in Fig. 1. The profiles are broadly distributed in longitude, so that each 60° arc contains at least four profiles and the largest gap in longitude between adjacent profiles is 33°. Within this set of observations, the uncertainty in T is typically ~0.4 K at the 610-Pa pressure level, a few kilometers above the surface, increasing to ~2 K at 50 Pa.

The discussion in this section illustrates two attributes of the RO measurements: their ability to resolve the vertical structure of shallow baroclinic waves and their sensitivity to the seasonal exchanges of CO_2 between the atmosphere and polar caps. In a subsequent section we will compare RO temperature profiles from group B with coordinated observations by the MRO MCS.

It is informative to evaluate these new results in the context of RO measurements acquired with MGS at ~60°N during $L_s = 20–25^\circ$ of MY 26 (30 May–9 June 2002). This 11-day span of observations yielded 109 profiles. The zonal distribution of the measurements is nearly uniform, with typically 8–10 profiles in each 30° arc of longitude. The temporal and spatial coverage of the MGS observations allows the properties of planetary-scale traveling waves to be determined with confidence, in contrast to the RO measurements with MRO.

There is a strong resemblance between the profiles from the two spacecraft, as shown in Fig. 13. Both sets of observations exhibit large temperature variations near the surface (500–900 Pa), where the difference between the warmest and coldest profiles exceeds 30 K. The variability within each set of profiles decreases markedly at higher altitudes. At pressures exceeding ~70 Pa the MRO profiles at 68°N are ~4 K colder on average than their counterparts from MGS at 60°N. This difference is expected for observations at this season, when temperatures at mid-to-high latitudes decrease toward the pole (Haberle et al., 1993; McCleese et al., 2010).

At the time of the observations in Fig. 13, near $L_s = 25^\circ$, the edge of the seasonal CO_2 ice cap typically has receded to ~63°N (James et al., 1999; Benson and James, 2003), midway between the latitudes sounded by MGS and MRO. The meridional gradient in surface temperature near the cap edge is conducive to baroclinic instability (James and Hoskins, 1985; Holton, 1992; James et al., 1999), and the large temperature variations observed by MGS in the lowest scale height above the surface arise primarily from an eastward-traveling baroclinic wave (Hinson, 2006).

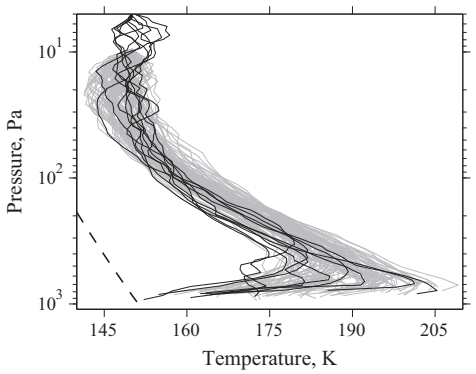

Fig. 13. Comparison of RO profiles from (gray) MGS and (black) MRO. The observations are from high northern latitudes in spring, ~60°N at $L_s = 20–25°$ of MY 26 for MGS, and ~68°N at $L_s = 23–28°$ of MY 30 for MRO. The MRO profiles generally lie within the temperature distribution of the more numerous MGS profiles. The dashed line is the saturation temperature of CO_2.

Motivated by the results in Fig. 13, we have re-examined this subset of MGS profiles, yielding a more complete description of the baroclinic wave that appears at this location and season in MY 26. The wave travels eastward with a period $P = 4.0$ sols and a zonal wave number $s = 2$. The temperature perturbations are confined to a shallow layer near the surface, as shown in Fig. 14, with a peak amplitude of ~10 K. The amplitude in geopotential height (not shown) is 160 m at the 610-Pa pressure level, and the configuration of the geopotential and temperature fields implies the presence of a net poleward eddy heat flux at pressures exceeding 400 Pa, with a peak value of ~30 K ms^{-1} near the surface. The procedure used to derive these results is explained in previous publications (Hinson, 2006; Hinson and Wang, 2010; Hinson et al., 2012).

The MGS TES observed a traveling wave with similar characteristics ($P = 4–5$ sols, $s = 2$) near the edge of the seasonal CO_2 ice cap in northern spring of both MY 24 and 25 (Banfield et al., 2004, Figs. 13 and 15). The wave mode exhibits the same spatial structure in both years, with the amplitude in temperature reaching its peak value near the surface at ~65°N. Taken together, the results derived from the MGS RO and TES observations suggest that the same wave mode recurs annually at this latitude and season, so that it might account for the large-amplitude temperature variations that appear near the surface in the recent RO measurements by MRO (Fig. 13).

We now turn our attention to RO measurements of geopotential height, which provide valuable constraints on the dynamical, seasonal, and interannual variations in the mass distribution of the atmosphere. Fig. 15 illustrates this point by comparing extensive measurements from MGS with the initial results from MRO. We consider only the geopotential height at 610 Pa, or Z_{610} for short, and we limit discussion to observations at high northern latitudes.

Fig. 15 was constructed using samples of Z_{610} from more than 8600 RO profiles, 22 from MRO and the rest from MGS. The 610-Pa pressure level is generally a few kilometers above the surface at the latitude of these observations, 55–85°N. The MGS results are from $L_s = 270°$ of MY 24 through $L_s = 270°$ of MY 26. The MRO results are from $L_s = 28–40°$ of MY 30, a seasonal window where the latitude coverage is closely aligned with previous measurements by MGS. The uncertainty in Z_{610} is typically ~30 m, barely discernible on the scale of Fig. 15.

The MGS measurements of Z_{610} follow a well-defined annual cycle with seasonal variations that exceed 2 km. Several processes determine its properties, including seasonal condensation and sublimation of CO_2 (Zurek et al., 1992), the seasonal evolution of the planetary-scale circulation (Hourdin et al., 1993, 1995), and the thermal expansion and contraction of the lowest few kilometers of the atmosphere, which also varies systematically with season. We characterized the net effect of these processes by binning the MGS data in 10° windows of L_s, computing the average value of Z_{610} within each of the 36 bins, and applying Fourier analysis to the results. (The MRO data were excluded from the fit.) We retained the first four terms in the series as a model for the annual cycle, as shown by the smooth curve in Fig. 15. Higher harmonics are insignificant, with amplitudes of order 10 m.

The RO measurements in Fig. 15 also provide an accurate record of synoptic-scale variations in the mass distribution of the atmosphere. The variance of Z_{610} with respect to the annual cycle arises from spatial and temporal modulation imposed by a combination of baroclinic waves – such as the one in Fig. 14 – and stationary Rossby waves, and their properties vary strongly with season (Hinson, 2006; Hinson and Wang, 2010; Hinson et al., 2012).

Most important, MRO has significantly extended the time span of the RO measurements of Z_{610}, increasing their sensitivity to subtle changes in the martian climate. According to the initial results from MRO, there has been no appreciable change in the annual cycle of Z_{610} during the span of 5 MY between the observations by MGS and MRO. A change of only 200 m in either direction would place all of the MRO samples of Z_{610} above or below the empirical fit to the MGS data, shown by the solid line in Fig. 15. This constrains any change in the annual cycle to be smaller than ~100 m in 5 MY, corresponding to a change in surface pressure of ~0.2% per MY.

A simple direct comparison of the results from the two spacecraft reinforces this conclusion. The MGS and MRO observations overlap at $L_s = 28–40°$, when the latitude range of the measure-

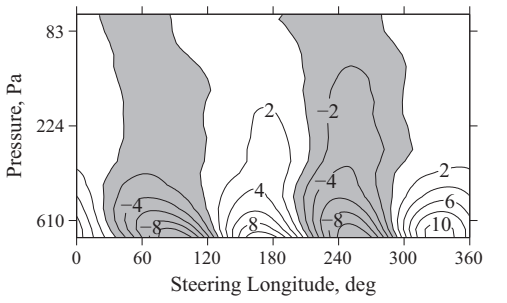

Fig. 14. MGS RO observations of temperature perturbations caused by a baroclinic wave at 60°N during $L_s = 20–25°$ of MY 26. The 'steering longitude' is the zonal coordinate in a reference frame moving eastward at 45° sol^{-1}, the zonal phase speed of the wave. The contour interval is 2 K, with shading for negative values. The bottom of the figure is ~1 km above the ground.

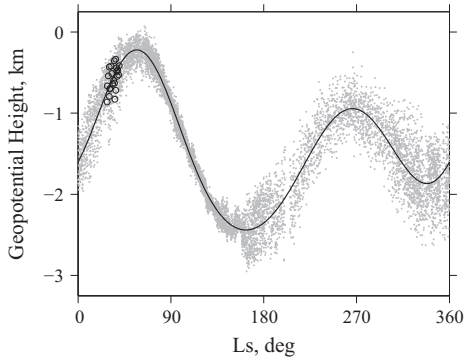

Fig. 15. Geopotential height at 610 Pa from RO measurements at high northern latitudes by (gray dots) MGS and (black circles) MRO. The MGS results are from $L_s = 270°$ of MY 24 through $L_s = 270°$ of MY 26. The MRO results are from $L_s = 28–40°$ of MY 30. The smooth curve is an empirical model for the annual cycle, as derived through Fourier analysis of the MGS data.

ments is 55–67°N for MGS and 58–67°N for MRO. These two subsets of data yield average values of Z_{610} that differ by less than 10 m. However, this result should be viewed with caution owing to the relatively small number of MRO observations (22) and their limited coverage in longitude.

Future measurements by MRO at mid-to-high northern latitudes in early northern summer, when the synoptic variability of Z_{610} is at its annual minimum, will provide a tighter constraint on any gradual increase or decrease in the active inventory of CO_2 on Mars.

4.3. Comparisons with results from the MRO MCS

The MRO MCS is a nine-channel, infrared, filter radiometer that measures thermal emission in limb, nadir, and intermediate 'off-nadir' viewing geometries (McCleese et al., 2007; Kleinböhl et al., 2009). The MCS has been observing the martian atmosphere since September 2006 ($L_s = 111°$ of MY 28), mapping the global temperature structure, the three-dimensional distributions of dust and water ice aerosols, and their variations on time scales from diurnal through interannual (McCleese et al., 2007, 2008, 2010; Kleinböhl et al., 2009, 2013; Lee et al., 2009; Heavens et al., 2010, 2011; Benson et al., 2011).

Neither nadir nor off-nadir observations are available for comparison with the RO profiles considered here. We therefore limit discussion to MCS measurements in the limb-viewing geometry, which yield profiles of temperature, dust opacity, and water ice opacity versus pressure (Kleinböhl et al., 2009, 2011). The vertical resolution is ~5 km. The vertical range of the temperature profiles is ~80 km, with a maximum pressure of ~300 Pa for the cases considered here. Limb observations are generally performed throughout each orbit, providing pole-to-pole coverage in latitude with regular sampling in longitude on both the dayside and the nightside.

As part of its standard sequence of observations, MCS also sounds the limb in the direction to Earth during the entry side of every RO measurement, except when prevented by pointing constraints. (The MCS field of view covers the limb over a 270° azimuth range but must remain more than 15° from the Sun for instrument safety.) These coordinated observations began in March 2009 ($L_s = 228°$ of MY 29), as shown in Fig. 1, intermediate to groups A and B of the RO observations.

The joint MCS-RO observations are implemented as follows. At occultation entry, the line of sight from spacecraft to Earth descends through the martian atmosphere at a rate of $\sim 10^3$ m s^{-1}, so that a single RO profile of the neutral atmosphere is retrieved from measurements lasting ~60 s. A single MCS limb profile requires a 25-s sequence of observations, and MCS typically repeats the sequence three times during each RO observation. The resulting trio of MCS limb profiles brackets the time and location of the RO profile, enabling a direct test of consistency.

Version 4.3 of the MCS retrievals – the one used here – will be delivered to the NASA PDS in mid 2014. This version benefits from improved knowledge of instrument pointing, which is important in the cross-track geometry of the observations considered here. In addition, there has also been a change in the criteria used to select channels for retrieval. A temperature profile is derived from measurements in three MCS channels (A1–A3), each with sensitivity over a different altitude range, and the algorithm for combining this information has been fine tuned in a way that reduces the impact of uncertainties in aerosol spectroscopy.

Coordinated observations by MCS are available for 21 of the RO profiles considered in this paper, all from group B at high northern latitudes in northern spring. We limit discussion to this subset of observations. Fig. 16 shows an example of the results. The comparison is bounded by the minimum RO pressure, ~5 Pa, and the maximum MCS pressure, ~200 Pa, a range of 3.7 pressure scale heights. The two versions of the RO retrieval differ only in the value adopted for T_b, the boundary condition at the top of the profile. In this set of MCS profiles, dust is confined to the lower atmosphere, at pressures greater than 80 Pa. Water ice is distributed over a deeper vertical range, with an opacity that exceeds 10^{-4} km^{-1} at pressures of 7–200 Pa. The MCS profiles end ~14 km above the surface, where the limb becomes opaque owing to the relatively large concentration of dust at low altitudes. (The RO measurements are insensitive to aerosols.) There are strong similarities between these RO and MCS temperature profiles, with particularly close agreement at pressures of 40–100 Pa.

It is important to consider the sensitivity of these comparisons to any misalignment of the MCS and RO observations. This does not appear to be a serious problem for the observations in Fig. 16. The alignment is good, and there is little variation among the three MCS profiles of temperature, dust, and opacity, so that horizontal gradients appear to be small at this location and season. The same conclusion applies to all coordinated observations from December 2009 and January 2010.

The results from all 21 comparisons are summarized in Fig. 17, which was constructed as follows. We used linear interpolation on a log-pressure vertical coordinate to estimate the RO temperature at each of the standard MCS pressure levels, which have a uniform separation of $H/8$, where H is the pressure scale height. We then subtracted the re-sampled RO profile from the appropriate MCS

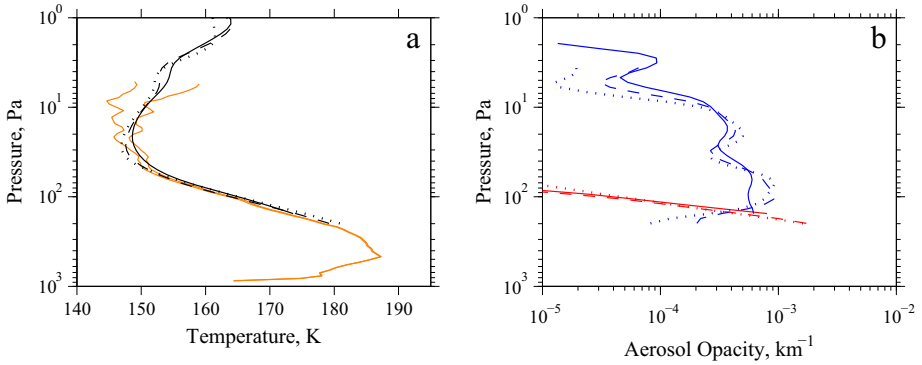

Fig. 16. Results from a set of concurrent RO and MCS observations at $L_s = 28.4°$ of MY 30 (25 December 2009). The panel at left shows (orange) RO and (black) MCS temperature profiles, while the panel at right shows MCS profiles of (blue) water ice opacity at 12 μm and (red) dust opacity at 22 μm, with opacity expressed as extinction per km. In this sequence of observations MCS sounded the atmosphere at (solid lines) 210°E, 68.5°N, (dashed lines) 209°E, 67.2°N, and (dotted lines) 208°E, 66.0°N. The RO observation was closely aligned with the second MCS profile. The local time was ~4.1 h. RO profiles are shown for two plausible values of T_b. (For interpretation of the references to color in this figure legend, the reader is referred to the web version of this article.)

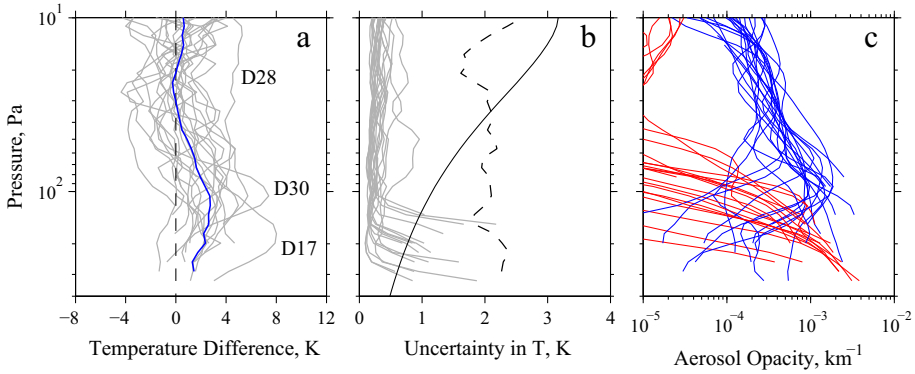

Fig. 17. Results from concurrent RO and MCS observations at 68–63°N in northern spring ($L_s = 24$–$35°$ of MY 30). (a) The gray lines show profiles of the temperature difference T_Δ for each of the 21 comparisons, while the heavy blue line shows their average value $\overline{T_\Delta}$. (b) The solid black line shows the average of the error estimate from the 21 RO profiles, while the gray lines show the random error associated with each of the 21 MCS profiles. The dashed line shows the standard deviation σ_Δ computed empirically from the temperature differences in (a). (c) MCS profiles of (blue) water ice opacity and (red) dust opacity for each of the 21 MCS retrievals. (For interpretation of the references to color in this figure legend, the reader is referred to the web version of this article.)

profile to obtain a difference profile T_Δ for each comparison. The results appear in Fig. 17a. We have excluded observations at pressures less than 10 Pa, where the RO retrieval depends strongly on the choice of T_b. (We set T_b to 155 K for all 21 comparisons.) For clarity, Fig. 17 shows results only for the second MCS profile within each set of coordinated observations.

Fig. 17b shows the formal uncertainties assigned to the MCS and RO profiles, as computed by the respective retrieval algorithms. (Their values are included in the data products delivered to the PDS.) For the MCS, the precision in temperature is typically smaller than 0.5 K at pressures of 10–100 Pa, increasing to 1–2 K near the base of each profile, where the dust opacity generally exceeds 10^{-3} km^{-1}. These random errors arise from measurement noise and radiance residuals; we consider the effect of uncertainties in aerosol spectroscopy later in this section. For the RO profiles, the precision in temperature is typically ~3 K at 10 Pa, decreasing to ~1 K at 100 Pa and 0.5 K at 400 Pa, as discussed in Section 3.2. Fig. 17b also shows the standard deviation σ_Δ computed empirically from the 21 difference profiles in Fig. 17a; its value is ~2 K independent of pressure.

It is instructive to discuss the results from these comparisons within two regimes, one where the ice and dust opacities retrieved by MCS remain smaller than 10^{-3} km^{-1} (10–50 Pa) and another where the opacities exceed this threshold (50–300 Pa).

Within the low-opacity regime, there is a high degree of consistency between the MCS and RO profiles, as reflected by an average difference in temperature $\overline{T_\Delta}$ of less than 1 K (Fig. 17a). The standard deviation σ_Δ is ~2 K, comparable to the precision of the RO profiles at pressures less than 50 Pa. Hence, the results at 10–50 Pa are consistent with the expected performance of the two instruments, with one possible exception. The RO profile from 28 December 2009 is ~5 K colder than its MCS counterpart, as shown in profile 'D28' of Fig. 17a, although the difference is not much larger than the uncertainty in this RO retrieval, 3–4 K at pressures of 10–50 Pa. Possible sources of a bias in this RO profile include a problem with trajectory reconstruction or anomalous motion of the spacecraft high-gain antenna, as noted in Section 3.1.

Within the high-opacity regime (50–300 Pa), MCS temperatures tend to be slightly warmer than RO temperatures, and the average temperature difference $\overline{T_\Delta}$ increases to about +2 K. This small bias is probably related to an increase in the concentration of aerosols – the ice opacity at 100 Pa is typically ~ 10^{-3} km^{-1}, and the dust opacity exceeds 10^{-3} km^{-1} at greater pressures, as shown in Fig. 17c. As the opacity approaches this threshold, MCS retrievals of temperature and pressure become sensitive to uncertainties in aerosol properties, such as the composition and refractive index of the dust particles as well as the shape and size distribution of both the dust and water ice particles (Kleinböhl et al., 2011). It is particularly important to know the spectroscopy of aerosols in the 15-μm band where temperature and pressure are retrieved. (The ice and dust opacities are retrieved at wavelengths of 12 and 22 μm, respectively.) The 2-K bias in $\overline{T_\Delta}$ at pressures greater than 50 Pa may reflect the impact of these uncertainties on the MCS retrievals.

The value of σ_Δ is ~2 K in the high-opacity regime, comparable to the combined precision of the RO and MCS retrievals. However, T_Δ exceeds σ_Δ by a significant margin within the comparisons on 17 and 30 December 2009, and these outliers deserve further discussion. In one case, profile 'D30' of Fig. 17a, T_Δ contains a localized anomaly with a peak value of +7 K at 106 Pa and a full width at half maximum of about $H/2$. Profile 'D17' exhibits a similar discrepancy centered at a somewhat larger pressure, 175 Pa. This type of anomaly can arise from uncertainties in aerosol spectroscopy, whose impact on the MCS retrieval is accentuated by the relatively large values of dust and ice opacity in the lower atmosphere at this latitude and season.

The results in Fig. 17 complement and extend previous work in this area, which compared MCS temperature retrievals with RO profiles from MGS (Kleinböhl et al., 2009; Shirley et al., 2014). As no contemporaneous observations were available, those comparisons relied on measurements from different martian years, and consideration was limited to the zonal-mean temperature structure. Both studies found good agreement between the MCS and RO measurements, with differences no larger than a few K, but the conclusions are limited by the possible presence of inter-annual variations. The results reported here confirm the findings of the previous studies while providing a more direct and less ambiguous cross-validation of the MCS and RO temperature profiles.

MRO continues to perform coordinated MCS and RO observations, allowing the comparisons to be extended to a broader range of atmospheric conditions. The objective is to identify any systematic differences between the MCS and RO profiles and to understand their origin, an important step toward improved performance by both sounders. These comparisons may lead eventually to a more confident characterization of martian weather and climate.

5. Availability of RO profiles

This paper reports the first detailed results derived from RO measurements with MRO. We have analyzed two groups of

observations, as summarized in Table 1, one from the tropics in summer and the other from high northern latitudes in spring. Each group of data has yielded ~50 profiles of the neutral atmosphere. While this paper was being reviewed and revised, we delivered another 83 profiles to the PDS, which will be the subject of future publications.

Acknowledgments

This research was funded in part by Grant NNX12AL48G (Hinson) of the Mars Data Analysis Program. We are grateful to Reta Beebe, Jim Murphy, and Lyle Huber for their support and guidance in archiving the RO profiles at the PDS Atmospheres Node.

References

Banfield, D., Conrath, B.J., Gierasch, P.J., Wilson, R.J., Smith, M.D., 2004. Traveling waves in the martian atmosphere from MGS TES nadir data. Icarus 170, 365–403.

Benson, J.L., James, P.B., 2003. Yearly comparisons of the Mars north polar cap: 1999, 2001, and 2003 MOC observations. In: Clifford, S., Doran, P., Fisher, D., Herd, C. (Eds.), Third International Conference on Mars Polar Science and Exploration. Lunar and Planetary Institute (LPI), p. 8097.

Benson, J.L., Kass, D.M., Kleinböhl, A., 2011. Mars' north polar hood as observed by the Mars Climate Sounder. J. Geophys. Res. (Planets) 116, 3008.

Colaprete, A., Toon, O.B., 2000. The radiative effects of martian water ice clouds on the local atmospheric temperature profile. Icarus 145, 524–532.

Fenton, L.K., Michaels, T.I., 2011. Mesoscale and large eddy simulations of dust devils in Amazonis Planitia, Mars. Lunar and Planetary Institute Science Conference Abstracts, vol. 42. Lunar and Planetary Institute (LPI), p. 2718.

Fjeldbo, G., Kliore, A.J., Eshleman, V.R., 1971. The neutral atmosphere of Venus as studied with the Mariner V radio occultation experiments. Astron. J. 76, 123–140.

Gill, A.E., 1982. Atmosphere-Ocean Dynamics. Academic Press, San Diego.

Haberle, R.M. et al., 1993. Mars atmospheric dynamics as simulated by the NASA AMES General Circulation Model: 1. The zonal-mean circulation. J. Geophys. Res. 98, 3093–3123.

Haberle, R.M. et al., 1999. General Circulation Model simulations of the Mars Pathfinder atmospheric structure investigation/meteorology data. J. Geophys. Res. (Planets) 104, 8957–8974.

Haberle, R.M. et al., 2011. Radiative effects of water ice clouds on the martian seasonal water cycle. In: Forget, F., Millour, E. (Eds.), Mars Atmosphere: Modelling and Observation. Laboratoire de Meteorologie Dynamique (LMD), pp. 223–226.

Heavens, N.G. et al., 2010. Water ice clouds over the martian tropics during northern summer. Geophys. Res. Lett. 37 (L18202), 18202.

Heavens, N.G. et al., 2011. Vertical distribution of dust in the martian atmosphere during northern spring and summer: High-altitude tropical dust maximum at northern summer solstice. J. Geophys. Res. (Planets) 116 (E01007), 1007.

Hinson, D.P., 2006. Radio occultation measurements of transient eddies in the northern hemisphere of Mars. J. Geophys. Res. (Planets) 111 (E05), E05002.

Hinson, D.P., Wang, H., 2010. Further observations of regional dust storms and baroclinic eddies in the northern hemisphere of Mars. Icarus 206, 290–305.

Hinson, D.P., Wilson, R.J., 2004. Temperature inversions, thermal tides, and water ice clouds in the martian tropics. J. Geophys. Res. (Planets) 109, E01002.

Hinson, D.P., Simpson, R.A., Twicken, J.D., Tyler, G.L., Flasar, F.M., 1999. Initial results from radio occultation measurements with Mars Global Surveyor. J. Geophys. Res. (Planets) 104 (E11), 26997–27012.

Hinson, D.P., Smith, M.D., Conrath, B.J., 2004. Comparison of atmospheric temperatures obtained through infrared sounding and radio occultation by Mars Global Surveyor. J. Geophys. Res. (Planets) 109 (E12), E12002.

Hinson, D.P., Pätzold, M., Tellmann, S., Häusler, B., Tyler, G.L., 2008a. The depth of the convective boundary layer on Mars. Icarus 198, 57–66.

Hinson, D.P., Pätzold, M., Wilson, R.J., Häusler, B., Tellmann, S., Tyler, G.L., 2008b. Radio occultation measurements and MGCM simulations of Kelvin waves on Mars. Icarus 193, 125–138.

Hinson, D.P., Wang, H., Smith, M.D., 2012. A multi-year survey of dynamics near the surface in the northern hemisphere of Mars: Short-period baroclinic waves and dust storms. Icarus 219, 307–320.

Hollingsworth, J.L., Kahre, M.A., Haberle, R.M., Montmessin, F., 2011. Radiatively-active aerosols within Mars' atmosphere: Implications on the weather and climate as simulated by the NASA ARC Mars GCM. In: Forget, F., Millour, E. (Eds.), Mars Atmosphere: Modelling and Observation. Laboratoire de Meteorologie Dynamique (LMD), pp. 70–73.

Holton, J.R., 1992. An Introduction to Dynamic Meteorology, third ed. Academic Press, San Diego.

Hourdin, F., Le Van, P., Forget, F., Talagrand, O., 1993. Meteorological variability and the annual surface pressure cycle on Mars. J. Atmos. Sci. 50, 3625–3640.

Hourdin, F., Forget, F., Talagrand, O., 1995. The sensitivity of the martian surface pressure and atmospheric mass budget to various parameters: A comparison between numerical simulations and Viking observations. J. Geophys. Res. 100, 5501–5523.

Howard, H.T. et al., 1992. Galileo radio science investigations. Space Sci. Rev. 60, 565–590.

James, I.N., Hoskins, B.J., 1985. Some comparisons of atmospheric internal and boundary baroclinic instability. J. Atmos. Sci. 42 (20), 2142–2155.

James, P.B., Hollingsworth, J.L., Wolff, M.J., Lee, S.W., 1999. North polar dust storms in early spring on Mars. Icarus 138, 64–73.

Jenkins, J.M., Steffes, P.G., Hinson, D.P., Twicken, J.D., Tyler, G.L., 1994. Radio occultation studies of the Venus atmosphere with the Magellan spacecraft: 2. Results from the October 1991 experiments. Icarus 110, 79–94.

Kahre, M.A., Hollingsworth, J.L., Haberle, R.M., Montmessin, F., 2011. Coupling Mars' dust and water cycles: Effects on dust lifting vigor, spatial extent and seasonality. In: Forget, F., Millour, E. (Eds.), Mars Atmosphere: Modelling and Observation. Laboratoire de Meteorologie Dynamique (LMD), pp. 143–146.

Kleinböhl, A. et al., 2009. Mars Climate Sounder limb profile retrieval of atmospheric temperature, pressure, and dust and water ice opacity. J. Geophys. Res. (Planets) 114 (E10), E10006.

Kleinböhl, A., Schofield, J.T., Abdou, W.A., Irwin, P.G.J., de Kok, R.J., 2011. A single-scattering approximation for infrared radiative transfer in limb geometry in the martian atmosphere. J. Quant. Spectrosc. Radiat. Transfer 112, 1568–1580.

Kleinböhl, A., Wilson, R.J., Kass, D., Schofield, J.T., McCleese, D.J., 2013. The semidiurnal tide in the middle atmosphere of Mars. Geophys. Res. Lett. 40, 1952–1959.

Konopliv, A.S., Yoder, C.F., Standish, E.M., Yuan, D.-N., Sjogren, W.L., 2006. A global solution for the Mars static and seasonal gravity, Mars orientation, Phobos and Deimos masses, and Mars ephemeris. Icarus 182, 23–50.

Lee, C. et al., 2009. Thermal tides in the martian middle atmosphere as seen by the Mars Climate Sounder. J. Geophys. Res. (Planets) 114 (E03005), 3005.

Madeleine, J.-B., Forget, F., Millour, E., Navarro, T., Spiga, A., 2012. The influence of radiatively active water ice clouds on the martian climate. Geophys. Res. Lett. 39 (L23202), 23202.

McCleese, D.J. et al., 2007. Mars Climate Sounder: An investigation of thermal and water vapor structure, dust and condensate distributions in the atmosphere, and energy balance of the polar regions. J. Geophys. Res. (Planets) 112 (E05), E05S06.

McCleese, D.J. et al., 2008. Intense polar temperature inversion in the middle atmosphere on Mars. Nat. Geosci. 1, 745–749.

McCleese, D.J. et al., 2010. Structure and dynamics of the martian lower and middle atmosphere as observed by the Mars Climate Sounder: Seasonal variations in zonal mean temperature, dust, and water ice aerosols. J. Geophys. Res. (Planets) 115 (E12), 12016.

Michaels, T.I., Rafkin, S.C.R., 2004. Large-eddy simulation of atmospheric convection on Mars. Q. J. R. Meteorol. Soc. 130, 1251–1274.

Pankine, A.A., Tamppari, L.K., Bandfield, J.L., McConnochie, T.H., Smith, M.D., 2013. Retrievals of martian atmospheric opacities from MGS TES nighttime data. Icarus 226, 708–722.

Shirley, J.H. et al., 2014. Temperatures and aerosol opacities of the Mars atmosphere at aphelion: Validation and inter-comparison of limb sounding profiles from MRO/MCS and MGS/TES. Icarus. http://dx.doi.org/10.1016/j.icarus.2014.05.011, in press.

Smith, D.E. et al., 2001. Mars Orbiter Laser Altimeter: Experiment summary after the first year of global mapping of Mars. J. Geophys. Res. (Planets) 106, 23689–23722.

Spiga, A., Forget, F., 2009. A new model to simulate the martian mesoscale and microscale atmospheric circulation: Validation and first results. J. Geophys. Res. (Planets) 114 (E2), E02009.

Spiga, A., Forget, F., Lewis, S.R., Hinson, D.P., 2010. Structure and dynamics of the convective boundary layer on Mars as inferred from large-eddy simulations and remote-sensing measurements. Q. J. R. Meteorol. Soc. 136, 414–428.

Tellmann, S., Pätzold, M., Häusler, B., Hinson, D.P., Tyler, G.L., 2013. The structure of Mars lower atmosphere from Mars Express Radio Science (MaRS) occultation measurements. J. Geophys. Res. (Planets) 118, 306–320.

Tyler, G.L., 1987. Radio propagation experiments in the outer Solar System with Voyager. IEEE Proc. 75, 1404–1431.

Tyler, G.L. et al., 2001. Radio science observations with Mars Global Surveyor: Orbit insertion through one Mars year in mapping orbit. J. Geophys. Res. (Planets) 106, 23327–23348.

Vasavada, A.R. et al., 2012. Assessment of environments for Mars Science Laboratory entry, descent, and surface operations. Space Sci. Rev. 170, 793–835.

Wilson, R.J., Guzewich, S.D., 2014. Influence of water ice clouds on nighttime tropical temperature structure as seen by the Mars Climate Sounder. Geophys. Res. Lett. 41, 3375–3381.

Wilson, R.J., Neumann, G.A., Smith, M.D., 2007. Diurnal variation and radiative influence of martian water ice clouds. Geophys. Res. Lett. 34 (L02710), 2710.

Wilson, R.J., Millour, E., Navarro, T., Forget, F., Kahre, M., 2014. GCM simulations of aphelion season tropical cloud and temperature structure. In: Forget, F., Millour, M. (Eds.), Mars Atmosphere: Modelling and Observation, 5th International Workshop. Laboratoire de Meteorologie Dynamique (LMD), pp. 1304–1307.

Zurek, R.W., Smrekar, S.E., 2007. An overview of the Mars Reconnaissance Orbiter (MRO) science mission. J. Geophys. Res. (Planets) 112 (E05), E05S01.

Zurek, R.W., Barnes, J.R., Haberle, R.M., Pollack, J.B., Tillman, J.E., Leovy, C.B., 1992. Dynamics of the atmosphere of Mars. In: Kieffer, H.H., Jakosky, B.M., Snyder, C.W., Matthews, M.S. (Eds.), Mars. Univ. of Arizona Press, Tucson, pp. 835–933.